

On the effects of Rayleigh number and inlet turbulence intensity upon the buoyancy-induced mass flow rate in sloping and convergent channels

B. Zamora, A.S. Kaiser*, A. Viedma

Dpto. Ingeniería Térmica y de Fluidos, Universidad Politécnica de Cartagena,
Doctor Fleming s/n, 30202 Cartagena, Spain

Abstract

A numerical study on the mass flow rate induced by natural convection in a sloped converging channel for different inclination and convergence angles with symmetrical heating has been reported. Two-dimensional, laminar, transitional and turbulent simulations were obtained by solving the fully-elliptic governing equations using two different general purpose codes: Fluent and Phoenics. In transitional and turbulent cases, the low-Reynolds $k - \omega$ turbulence model has been employed. Special emphasis has been carried out, for turbulent regime, on the systematic comparisons of computational results with experimental and numerical data taken from literature, considering the influence of inlet turbulence intensity upon transitional point. Numerical results were obtained for wide and not yet covered ranges of the modified Rayleigh number varying from 10^{-2} to 10^{12} , the aspect ratio between 0.03 to 0.25, the converging angle from 1° to 30° and sloping angle from 0° to 60° . A generalized correlation for the non-dimensional mass flow rate has been obtained from numerical results in a channel with isothermal plates, for symmetric heating conditions.

Keywords: Convective flows, sloped converging channels, turbulence intensity.

*Corresponding author. Fax no.: +34 968 325 999. E-mail: antonio.kaiser@upct.es

Notation

b	minimum inter-plate spacing in the channel (Fig. 1)
c_p	specific heat at constant pressure
g	gravitational acceleration
Gr	Grashof number for isothermal cases, $g\beta(T_w - T_\infty)l^3/\nu^2$
Gr	Grashof number for heat flux cases, $g\beta ql^4/\nu^2\kappa$
h_χ	local heat transfer coefficient, $\kappa(\partial T/\partial y)_w/(T_w - T_\infty)$
I	turbulence intensity, Equation (15)
k	turbulent kinetic energy, Equation (5)
L	streamwise length of wall (Fig. 1)
l	typical length, $l = L$ or $l = b$
\dot{m}	two-dimensional mass flow rate
Nu_b	average Nusselt number based on b
Nu_L	average Nusselt number based on L , Equation (18)
Nu_χ	local Nusselt number, $h_\chi\chi/\kappa$
P	average reduced pressure
Pr	Prandtl number, $\mu c_p/\kappa$
q	wall heat flux
Ra	Rayleigh number, $(Gr)(Pr)$
Ra^*	modified Rayleigh number based on b , $Ra_b(b/L)$
Re	Reynolds number, Ul/ν
T	average temperature
T'	turbulent temperature
T_w	wall temperature
T_∞	ambient temperature
U	typical velocity
$-\overline{T'u_j}$	averaged turbulent heat flux
U_j	average components of velocity
u_j	turbulent components of velocity
$-\overline{u_i u_j}$	turbulent stress
u_τ	friction velocity $u_\tau = (\tau_w/\rho)^{1/2}$
x, y, z	cartesian coordinates (Fig. 1)

y^+ $\rho y u_\tau / \mu$, with y the distance between the wall and the first grid point

Greek symbols

β coefficient of thermal expansion, $1/T_\infty$
 γ converging angle (Fig. 1)
 Θ inclination angle (Fig. 1)
 κ thermal conductivity
 μ viscosity
 ν kinematic viscosity, μ/ρ
 ρ density
 Φ non-dimensional mass flow rate based on b , $\Phi = \dot{m}/\rho\nu Gr_b$
 χ coordinate along the wall (Fig. 1)
 τ_w wall shear stress
 ω specific dissipation rate of k (or turbulent frequency)

Subscripts

bl boundary-layer limit
 fd fully developed limit
 t turbulent
 w wall
 ∞ ambient or reference conditions

Superscripts

— averaged value

1 Introduction

Free convection phenomena plays an important role in design and performance of different problems, like naturally ventilated buildings or cooling of electronic components. Its influence on the performance is very significant in many cases. For example, inducing higher mass flow rate results into obtaining better mixing in typical room ventilation applications. The geometries studied frequently involve structures based on converging and sloped channels formed by heated plates, where buoyancy-driven flows take place. So, the study of laminar and turbulent buoyancy-induced flows in these devices by a generalized geometry may be considered interesting from a fundamental point of view. A large number of works published on laminar natural convection flow in channels exists; however, only few researches were reported on the turbulent case. As a consequence of the great scale of certain passive ventilation systems, as solar chimneys, Trombe walls or roof collectors, the flow established becomes transitional or even fully turbulent. In addition, important lacks over correlations for the buoyancy-induced mass flow rate have been detected. Thus, the main objective became for the present work to obtain a generalized correlation for the mass flow rate as a function of Rayleigh number, taking into account the effects of several geometrical parameters. This correlation could be employed in sizing methods of passive ventilation systems, for a given conditions.

As pointed before, a limited number of turbulent investigations on the problem outlined has been reported. Some relevant researches are exposed following. Lloyd and Sparrow [1] analyzed the conditions of transition to turbulence for a flow induced by natural convection in an isolated vertical plate and they reported a value for the turbulence transition of Grashof number (based on the length of channel L) of 1.24×10^9 . Miyamoto et al. [2] studied experimentally turbulent flows in vertical channels formed by one of the plates with a constant heat flux and the other plate as adiabatic. They established the transition for a local Grashof number in the order of 10^{13} .

Yuan et al. [3] proposed wall functions for numeric simulations of turbulent convective flows in vertical plates. Versteegh and Nieuwstadt [4] studied the scaling behavior of natural convection flows to propose wall functions for natural convection flows between two infinite differentially heated vertical walls. Henkes and Hoogendorn [5] analyzed turbulent convection in enclosures, stating as other authors the difficulties found in some turbulence models, such as the standard $k - \epsilon$.

Peng and Davison [6] employed the $k - \omega$ turbulence model to describe the turbulent flow induced by natural convection within a cavity. Xu et al. [7] analyzed the flow established by buoyancy effects in a channel through a new model of turbulence which uses direct numerical simulation (DNS) in the region close to the wall and also they utilized the model $k - \epsilon$ for the region further away from the wall. Said et al. [8] studied the same problem for modified Rayleigh numbers (based on width of the channel, b) between 10^4 and 10^6 , and sloping angles of the channel, between 0° and 90° , through a modified $k - \epsilon$ turbulence model.

Fedorov and Viskanta [9] employed the low-Reynolds number $k - \epsilon$ turbulence model to calculate the induced flow and heat transfer in an asymmetrically heated, vertical parallel-plate channel. They have compared their results with those obtained experimentally by Miyamoto et al. [10]. These authors reported that the turbulence intensity at the channel inlet affects the location of transition from laminar to turbulent flow. Their results indicated that increasing turbulence intensity at the channel inlet causes the flow to be turbulent at downstream section. Furthermore, this behavior influenced the rate of heat transfer.

Although a large number of studies on natural convection heat transfer in vertical channels have been reported, the induced mass flow rate has not deserve the same attention. Hajji and Worek [11] have proposed an analytical solution to fully developed flow in a sloped channel. Lee [12] has investigated analytically and experimentally the effects of considering unheated extensions at inlet or outlet of a vertical channel. Following works of Aung [13], Nelson and Wood [14] have determined both heat transfer and air mass flow within vertical channels with asymmetric heating conditions.

As it could be expected, the 'burnout' effects described by Guo and Wu [15] and Hernández and Zamora [16] can not appear in our computations, for the range of parameters and heating conditions studied. However, their investigations deserve the following description. For laminar flow and symmetrical heating, Guo and Wu [15] carried out a research into the influence of variable property effects on the air flow induced by natural convection. They also showed that the effects of density variations lead to a non-monotonic dependence of the mass flow rate obtained on the channel (since air density decreases when temperature increases, this behavior is so-called 'thermal drag'). When the temperature fixed at wall or the heat flux imposed increase, after an ascendent trend, the mass flow rate trends to diminish after a certain maximum value. Indeed, when the wall heat flux is fixed and reaches a certain critical value, the wall temperature increases suddenly and shows a critical behavior, simi-

lar to burnout phenomena in flow boiling cases. Hernández and Zamora [16] investigated the influence of variable property effects on natural-convection laminar air flows in vertical channels under non-uniform heating and non-Boussinesq conditions. They have carried out an analytical estimation of the critical wall heat flux, and they have compared their results with those obtained by Guo and Wu [15].

In view of these studies it can be observed that most of the results reported were obtained for heat transfer parameters, while mass flow rate has deserved a minor attention mainly for turbulent regime, as aforementioned. Indeed, this work is focused on the study of induced flow by natural convection in convergent and inclined channels (described on Figure 1) in the laminar, laminar-turbulent transition and fully turbulent regimes with symmetrical isothermal heating, and aimed mainly on the induced mass flow rate through the channel.

The first part of the paper has been focused on laminar flow. In the second one, the study of transitional and turbulent flow has been broached, with special attention on the influence of turbulence intensity imposed at the inlet of the channel. The governing equations and turbulence model are introduced in next section. Since our objective is to analyze the effects of Rayleigh number and initial turbulence intensity, principally over the induced mass flow rate, Boussinesq approximation and uniform properties for air have been considered. The numerical solution procedure for the full Navier-Stokes elliptic equations is also exposed. Numerically, turbulent models as the standard $k - \epsilon$, in combination with wall functions has been usually applied. Contrary to forced convection boundary layers, at the moment typical logarithmic wall functions seem to be not appropriate to calculate the natural convection boundary layer. In this way, the low-Reynolds $k - \omega$ turbulence model have been employed to solve the cases considered in present research. The flow has been assessed by using the Fluent and Phoenics codes, both based on a finite volume procedure. These codes have been validated enough to solve natural convective flows. Successfully laminar results have been obtained by authors in Kaiser et al. [17]. The working fluid is air, with a constant Prandtl number equal to 0.71. As it could be expected, the computational results obtained with Fluent and Phoenics have been almost coincidental. However, some slight differences will be exposed. Finally, in *Discussion of results*, validation of numerical results, influence of sloping and converging angles, so as so the effects of initial turbulence intensity, and a generalized correlation for the mass flow rate are explained.

2 Mathematical model

2.1 Governing equations

Since the temperature variations are not too high, the Boussinesq approximation can be employed, assuming constants the thermophysical properties of the fluid, except for density variations in the buoyancy term in the vertical momentum equation. Applying this approximation, the simplified time-averaged Navier-Stokes equations of motion for steady, two-dimensional incompressible flow, can be written as follows:

$$\frac{\partial U_j}{\partial x_j} = 0, \quad (1)$$

$$\left(\frac{\partial U_i U_j}{\partial x_j} \right) = -\frac{1}{\rho} \frac{\partial P}{\partial x_i} - g_i \beta (T - T_\infty) + \frac{\partial}{\partial x_j} \left(\nu \frac{\partial U_i}{\partial x_j} - \overline{u_i u_j} \right), \quad (2)$$

$$\frac{\partial (T U_j)}{\partial x_j} = \frac{\partial}{\partial x_j} \left(\frac{\nu}{\text{Pr}} \frac{\partial T}{\partial x_j} - \overline{T' u_j} \right), \quad (3)$$

where U is the average velocity, T the average temperature, and P the average reduced pressure, difference between the pressure and the ambient pressure P_∞ (this given by the hydrostatic law, $dP_\infty/dx = -g\rho_\infty$); β is the thermal expansion coefficient (equal to $1/T_\infty$ for a perfect gas). The turbulent stress $-\overline{u_i u_j}$ and turbulent heat flux $-\overline{T' u_j}$ are supplied from the turbulence closure model, which are explained below, assuming that

$$-\overline{u_i u_j} = 2\nu_t S_{ij} - \frac{2}{3}k\delta_{ij}, \quad \text{and} \quad -\overline{T' u_j} = \frac{\nu_t}{\text{Pr}_t} \frac{\partial T}{\partial x_j}, \quad (4)$$

being ν_t and Pr_t the turbulent kinematic viscosity and turbulent Prandtl number, respectively; S_{ij} is the mean strain tensor, $S_{ij} = [(\partial U_i/\partial x_j) + (\partial U_j/\partial x_i)]/2$, δ_{ij} the Kronecker delta, and k de kinetic turbulent energy,

$$k = \frac{\overline{u_x^2} + \overline{u_y^2} + \overline{u_z^2}}{2}. \quad (5)$$

Obviously, for fully laminar flow, $-\overline{u_i u_j} = -\overline{T' u_j} = 0$. Moreover, radiation effects are neglected.

2.2 Turbulence model

The closure problem posed in Equations (1), (2) and (3) (also called Reynolds-averaged equations) is solved through the two transport equations $k - \omega$ model. This model has some advantages in transitional flows. Indeed, no additional models have been employed to lead the

flow to transition at certain location in the flow field; in this way, the transition point takes place as a part of the solution of governing transport equations. Another advantage of the model is that it does not imply an excessively high computational cost, even using the low-Reynolds version model. For example, it does not require the calculation of wall distances or damping functions based on the friction velocity.

The $k - \omega$ model proposed by Wilcox [18] has been used in the present study mainly because it includes a low-Reynolds number extension for near-wall turbulence and allows the simulation of transitional flows. The first turbulence model of two transport equations was the $k - \omega$ model, proposed originally by Kolmogorov [19]. This model involves equations for the transport of kinetic turbulent energy, k , and for the specific dissipation ω , defined as the ratio between the dissipation rate of k , and the same k . The $k - \omega$ transport equations model can be derived from the Navier-Stokes equations and it can be written as follows:

1. Transport equation for kinetic turbulent energy k ,

$$U_j \frac{\partial k}{\partial x_j} = \frac{\partial}{\partial x_j} \left[\left(\nu + \frac{\nu_t}{\sigma_k} \right) \frac{\partial k}{\partial x_j} \right] + \overline{u_i u_j} \frac{\partial U_i}{\partial x_j} - \beta^* f_{\beta^*} k \omega. \quad (6)$$

- In the diffusion term, the effective diffusivity is $\nu + (\nu_t/\sigma_k)$, and the kinematic eddy viscosity is given by

$$\nu_t = \alpha^* \frac{k}{\omega}, \quad (7)$$

being α^* a function that damps the turbulent viscosity causing a low-Reynolds number correction, given by

$$\alpha^* = \alpha_\infty^* \left(\frac{\alpha_0^* + \text{Re}_t/R_k}{1 + \text{Re}_t/R_k} \right), \quad \text{with } \text{Re}_t = \frac{k}{\nu \omega}. \quad (8)$$

- The turbulence production term is $\overline{u_i u_j} (\partial U_i / \partial x_j)$.
- In the turbulence dissipation term, $-(\beta^* f_{\beta^*} k \omega)$, the factor f_{β^*} is

$$f_{\beta^*} = \begin{cases} 1, & \xi_k \leq 0 \\ \frac{1+680\xi_k^2}{1+400\xi_k^2}, & \xi_k > 0 \end{cases}, \quad \text{with } \xi_k \equiv \frac{1}{\omega^3} \frac{\partial k}{\partial x_j} \frac{\partial \omega}{\partial x_j}, \quad (9)$$

and β^* is a damping function of Re_t ,

$$\beta^* = \beta_\infty^* \left(\frac{4/15 + (\text{Re}_t/R_\beta)^4}{1 + (\text{Re}_t/R_\beta)^4} \right). \quad (10)$$

The optative additional production of turbulent buoyancy, $-g_i \beta (\nu_t / \text{Pr}_t) (\partial T / \partial x_i)$, have been neglected, since no stratification temperature fields is expected in the present work.

2. Transport equation for specific dissipation rate or turbulence frequency ω ,

$$U_j \frac{\partial \omega}{\partial x_j} = \frac{\partial}{\partial x_j} \left[\left(\nu + \frac{\nu_t}{\sigma_\omega} \right) \frac{\partial \omega}{\partial x_j} \right] + \overline{u_i u_j} \frac{\partial U_i}{\partial x_j} \alpha \frac{\omega}{k} - \beta f_\beta \omega^2. \quad (11)$$

- In the production term, $\overline{u_i u_j} (\partial U_i / \partial x_j) \alpha (\omega / k)$, α is another damping function,

$$\alpha = \frac{\alpha_\infty}{\alpha^*} \left(\frac{\alpha_0 + \text{Re}_t / R_\omega}{1 + \text{Re}_t / R_\omega} \right). \quad (12)$$

- In the dissipation term $-(\beta f_\beta \omega^2)$, f_β is:

$$f_\beta = \frac{1 + 70 \xi_\omega}{1 + 80 \xi_\omega}, \quad \text{with} \quad \xi_\omega \equiv \left| \frac{\Omega_{ij} \Omega_{jk} S_{ki}}{(\beta_\infty^* \omega)^3} \right|, \quad (13)$$

being Ω_{ij} and S_{ki} the mean-rotation and mean-strain tensors, respectively given by

$$\Omega_{ij} = \frac{1}{2} \left(\frac{\partial U_i}{\partial x_j} - \frac{\partial U_j}{\partial x_i} \right), \quad S_{ij} = \frac{1}{2} \left(\frac{\partial U_i}{\partial x_j} + \frac{\partial U_j}{\partial x_i} \right). \quad (14)$$

It can be deduced that the factor ξ_ω is zero for two-dimensional flows, and so, $f_\beta = 1$.

The following experimental constants complete the model: $R_k = 6.0$, $\alpha_0^* = \beta_i / 3$, $\alpha_\infty^* = 1$, $\beta_i = 0.072$, $R_\beta = 8.0$, $\beta_\infty^* = 0.09$, $\sigma_k = \sigma_\omega = 2.0$, $R_\omega = 2.95$, $\alpha_\infty = 0.52$, $\alpha_0 = 1/9$, $\beta = \beta_i$. A constant value of $\text{Pr}_t = 0.86$ for air was assumed in the computations. A more detailed description of $k - \omega$ turbulence model can be found in Wilcox [18]. As pointed above, the turbulent $k - \omega$ model used in the present study was capable to determine descriptively the transitional point (from laminar to turbulent flow).

2.3 Near-wall settings

According to the universal behavior near the wall, some turbulence models impose in this region the so-called 'wall functions' which simulate above behavior; in this way, the flow is not solved in this zone. This could be appropriate in fully turbulent flows. However, in transitional flows, the turbulence production does not have to balance itself with the turbulence dissipation close the walls, and the hypothesis of universality of the boundary layer profiles (the 'law of the wall', usually logarithmic) is not fulfilled. The $k - \omega$ model allows to use wall functions when mesh is sufficiently coarse near the wall, with $y^+ > 30$, or otherwise, to solve the flow within viscous sub-layer when the mesh becomes sufficiently fine and includes some nodes inside the viscous sub-layer, with non-dimensional sub-layer scaled distance $y^+ \approx 1$.

2.4 Boundary conditions

At *inlet section*, the average reduced total-pressure imposed is $P_T = P + \rho(U_x^2 + U_y^2)/2 = 0$. The air temperature is fixed equal to the ambient temperature T_∞ . Since k - and ω -equations are homogenous, initial values of k and ω must be imposed to start computations. Indeed, the initial values for turbulent kinetic energy k is imposed by the way of a turbulence intensity, defined as follows:

$$I = \frac{[(2/3)k]^{1/2}}{\bar{U}}, \quad (15)$$

where \bar{U} is the main average velocity at the channel inlet. Thus, at inlet,

$$k_{inlet} = \frac{3}{2}I^2\bar{U}^2, \quad \omega_{inlet} = \frac{k_{inlet}}{\nu_t}. \quad (16)$$

Turbulent intensity I is comprised between 2% and 30% in all the outlined cases. In order to obtain correlations for the induced mass flow rate, I is limited to 2%. Under certain conditions, conduction effects at inlet could be important. For laminar flows, Hernández et al. [20] have studied the effect of including an entrance region to the domain. They reported that an extended computational domain at inlet is required only for cases with very low Rayleigh numbers. In this work, the diffusion effects at the channel inlet is neglected.

At *outlet section*, it is considered that the average reduced pressure is $P = 0$. Since an initial value of velocity at inlet section is not known *a priori* in natural convection flows, a reference level for pressure is necessary for the elliptic numerical simulation of problem outlined. Assuming that the flow discharges in a jet-like manner to the ambient at exit, the streamwise variations of velocity components, temperature, turbulent kinetic energy and turbulence frequency are neglected.

At *walls*, the no-slip boundary conditions is imposed on the average and turbulent velocity components. In isothermal cases, it is considered a fixed temperature with a value $T = T_w$; at walls with a fixed heat flux q , it is imposed $\kappa(\partial T/\partial y) = q$, with y the cross coordinate, and at adiabatic walls, $\partial T/\partial y = 0$. For turbulent cases, $k = 0$ is imposed, and by means of a balance for the ω -equation, an asymptotic expression for ω as the wall is approached [18],

$$k = 0, \quad \omega = \frac{K\nu}{\beta_\infty^* y^2}, \quad (17)$$

being the theoretical value for K of 2. The value for ω given by Equation (17) is employed to calculating ω at the computational first point adjacent to the wall surface.

3 Numerical computations

Results presented in this work have been obtained by using both the general-purpose Fluent and Phoenics codes, based on a finite volume procedure. In Fluent, the equations are discretised on a staggered grid, using the 'Presto' scheme, which is similar to the staggered-grid scheme employed in Phoenics, with a second-order scheme for the convective terms. The Simple algorithm of Patankar and Spalding [21] is employed to solve the coupling between continuity and momentum equations through pressure. In Phoenics, the results have been achieved employing a second-order differential scheme of 'Muscl' type for the convective terms [22]. The authors have verified that using of alternative differential schemes has produced nearly identical results. The convergence criterion in each case was $(\phi^{i+1} - \phi^i)/\phi^i \leq 10^{-5}$, where i denotes iteration number and ϕ can stand for any of the dependent variables.

In both Fluent and Phoenics codes, the turbulence model $k - \omega$ described previously has been implemented. As a competitive advantage, the $k - \omega$ turbulence model revealed to be convergent enough in this work, for the wide range of Rayleigh number studied.

A structured, non-uniform mesh has been built in both codes. The accuracy of the numerical results was tested by a grid dependence study. For laminar flow, a non-uniform grid consisting of 120 cells in the x direction and 80 cells in the y direction has been employed in most of cases. For both the horizontal and vertical direction, and for each grid and aspect ratio, power-law distribution was used to obtain a fine grid near walls, as well as inlet and outlet sections of the channel. For transitional and turbulent flow, two parameters have been considered to analyze the influence of the grid size on the mass flow rate: the y^+ and the number of cells in x and y directions. Figure 2 shows the results of this grid independence study for a convergent channel with $Ra^* = 10^9$, aspect ratio $b/L = 0.1$, converging angle $\gamma = 12^\circ$ and inclination angle $\Theta = 0^\circ$, for y^+ varying between 0.09 and 123, and different grid sizes (64×48 , 96×72 , 120×80 , 128×96 , 176×132 , 240×180 , 280×210 and 400×300). For each grid size, the different values of y^+ have been obtained by imposing different power-law distributions in y direction. As it could be appreciated in this figure, for $y^+ \geq 2$, non-dimensional mass flow rate is affected mainly by the y^+ value and slightly by the number of cells, for each value of y^+ . For values of y^+ lower than 2, this influence practically disappears and grid independence results are obtained. Following this study, the results presented in this work have been calculated using a non-uniform grid that gets y^+ lower than unity, including at least 10 grid points in the viscous sub-layer. Since ω values computed at the first grid node close to

the wall are very high, strong relaxation factors for turbulent variables was employed to get enough accurate solutions.

4 Discussion of results

Numerical results have been obtained for modified Rayleigh number $10^{-2} \leq Ra^* \leq 10^{12}$, aspect ratio between $0.03 \leq b/L \leq 0.25$, converging angle $1 \leq \gamma \leq 30^\circ$ and sloping angle $0 \leq \Theta \leq 60^\circ$. First, laminar flow has been broached. Second, transitional and turbulent flows has been studied, with special attention on the influence of initial turbulence intensity.

Nusselt number has been calculated as follow:

$$Nu_L = \frac{1}{L} \int_0^L Nu_\chi d\chi, \quad \text{with } Nu_\chi = h_\chi \chi / \kappa, \quad (18)$$

where h_χ is the local heat transfer coefficient and L the length of the channel. Obviously, χ coordinate along the wall is equal to x for a parallel channel. If average Nusselt number is based on b , Nu_b , then $Nu_{b,\chi} = h_\chi b / \kappa$.

On the other hand, the non-dimensional mass flow rate have been defined as:

$$\Phi = \frac{\dot{m}}{\rho v Gr_b}, \quad (19)$$

with \dot{m} is the two-dimensional mass flow rate, and $Gr_b = g\beta(T_w - T_\infty)b^3/\nu^2$ the Grashof number based on b .

First part: LAMINAR FLOW

Figure 3 shows the results obtained for mass flow rate induced in a vertical channel ($\gamma = \Theta = 0^\circ$), for a wide range of modified Rayleigh number, $Ra^* = (Gr_b)(Pr)(b/L)$, and values of aspect ratio equal to $b/L = 0.03$ and 0.1 . As expected, two different trends have been obtained: fully-developed (*fd*) regime for low enough Ra^* , and boundary-layer (*bl*) regime, for high enough Ra^* . There is an excellent agreement between numerical results and the asymptotical solution given by Hajji and Worek [11]:

$$\Phi_{fd} = \Phi_\infty \left[1 - \left(\frac{1}{24} \right) \Phi_\infty Ra^* / Pr \right], \quad (20)$$

with Φ_∞ the value of Φ_{fd} when $b/L \rightarrow 0$, equal to $1/12$. For values of Ra^* between 10^{-2} and 1 , deviation of numerical results with regards to above expression was of 1 %. In boundary

layer regime, although dimensional mass flow rate \dot{m} increases as Ra^* increases, that augmentation is lower than the increasing of buoyancy forces (i.e., Grashof number). In this way, dimensionless mass flow rate Φ decreases when Ra^* increases, as it could be appreciated in Figure 3. The results obtained were fitted to following expression:

$$\Phi_{bl} = \mathcal{A}(Ra^*)^{\mathcal{B}}, \quad (21)$$

with $\mathcal{A} = 0.967$ and $\mathcal{B} = -0.646$. For $10^3 \leq Ra^* \leq 10^5$, deviation was about 7 %. Taking into account the non-dimensional parameters defined above, results obtained were almost independent on channel aspect ratio b/L .

4.1 Influence of sloping angle

For the cases studied in this research, the influence of sloping angle is taken into account including the factor $(\cos \Theta)$ in the definition of the Rayleigh number. Said et al. [8] have proposed the factor $(\cos \Theta)^{0.5}$. These authors extended their study to sloping angles of 90° . The utilization of Rayleigh number based on $(\cos \Theta)$ factor means the assumption of a widely employed practice for inclined plates. In a converging or sloping channel, the buoyancy force is no longer solely in the streamwise direction, since a component also exists perpendicular to the heated wall. Thus, the specific buoyancy force that accelerates the fluid in the thermal boundary layer is $[g\beta(T_w - T_\infty) \cos \Theta]$ instead of $[g\beta(T_w - T_\infty)]$. Later on, a correlation for the case of fully turbulent flow, which includes both the sloping angle (Θ) and the convergence angle of the plates (γ), will be exposed. The specific buoyancy force is $[g\beta(T_w - T_\infty) \cos \Theta \cos \gamma]$ in the last case.

In order to study the influence of a sloping angle regards to vertical axis, cases made with $\Theta = 15^\circ, 30^\circ, 45^\circ$ and 60° , and aspect ratio $b/L = 0.03$ and 0.1 were computed. Results have been compared with those obtained by Hajji and Worek [11] for dimensionless mass flow rate, and a good agreement was found, as shows Figure 3, where Ra^* is modified through $(\cos \Theta)$. Once again, the influence of aspect ratio results almost negligible. In a similar way that above, the boundary-layer correlation for Φ can be written as:

$$\Phi_{bl} = \mathcal{A}(Ra^* \cos \times)^{\mathcal{B}}, \quad (22)$$

fitting also with $\mathcal{A} = 0.967$ and $\mathcal{B} = -0.646$, for $10^3 \leq Ra^* \leq 10^5$ and a deviation about 7%.

4.2 Influence of converging angle

For converging and sloping channels, best correlation of results obtained was reached by using the minimum inter-plate spacing to describe the problem in study [17]. It can be observed in Figure 4 that numerical results do not follow the same asymptotical fully-developed behavior at low enough Ra^* for different values of γ . For converging channel, with dimensionless governing parameters based on minimum inter-plate spacing, m increases as well as converging angles does, for a low enough Ra^* . The reason for that might be the augmentation of fluid volume under buoyancy force. In a previous work, Kaiser et al. [17], an asymptotic correlation for average Nusselt number and for fully-developed regime was obtained by the assumption of differential body forces over the flow field. As reported in that previous work, the relative increase of specific buoyancy force with respect to a vertical parallel channel of $b \times L$ dimensions was proportional to $(\cos\gamma)(\sin\gamma)$. Taking this into account, next expression

$$\Phi_{fd} = \Phi_{\infty} \left[1 + 3.0 \frac{(\cos\gamma)^2(\sin\gamma)}{\Phi_{\infty}} \right], \quad (23)$$

adjust accurately to numerical results, for low enough Ra^* , with $\Phi_{\infty} = 1/12$, as pointed above.

On the other hand, the boundary-layer expression for dimensionless mass flow rate takes the form:

$$\Phi_{bl} = \mathcal{A}(Ra^* \cos\gamma)^{\mathcal{B}}, \quad (24)$$

fitting with $\mathcal{A} = 0.967$ and $\mathcal{B} = -0.646$, as expected, for $10^3 \leq Ra^* \leq 10^5$ and also a deviation about 7 %.

4.3 Influence of slope and converging channels

To find the combined influence of both sloping and converging angles, additional computations for $\Theta = 15^\circ, 30^\circ, 45^\circ$ and 60° , for $\gamma = 15^\circ$ and $\gamma = 30^\circ$ were carried out. The overlapping of results obtained (see Figure 5, for $\gamma = 30^\circ$ and $b/L = 0.1$) taken place by changing Ra^* by $Ra^*(\cos\Theta)(\cos\gamma)$. In this way, for boundary-layer regime ($10^3 \leq Ra^* \leq 10^5$),

$$\Phi_{bl} = \mathcal{A}(Ra^* \cos\Theta \times \cos\gamma)^{\mathcal{B}}, \quad (25)$$

closed obviously with $\mathcal{A} = 0.967$ and $\mathcal{B} = -0.646$, as the cases corresponding to $\gamma = \Theta = 0^\circ$. In order to simplify, the slight influence of b/L on coefficients \mathcal{A} and \mathcal{B} was neglected. The effects of b/L will be retained on the blended-correlation exponent n , described later.

4.4 Generalized correlation proposed

According to numerical results presented in this paper for laminar flow, a correlation was determined both for fully-developed and for boundary-layer regimes, by using the general expression suggested by Churchill and Usagi [23],

$$\Phi = [\Phi_{fd}^n + \Phi_{bl}^n]^{1/n}, \quad (26)$$

where n is a blended coefficient. The global correlation takes the form (see Figure 6):

$$\Phi = \left\{ \left[\Phi_{\infty} \left(1 + 3.0 \frac{(\cos \gamma)^2 (\sin \gamma)}{\Phi_{\infty}} \right) \right]^n + \left[0.967 (\text{Ra}^* \cos \Theta \cos \gamma)^{-0.646} \right]^n \right\}^{1/n}. \quad (27)$$

The value of the exponent n was obtained by correlating the numerical results obtained in this work. This coefficient, as a function of b/L and γ , may be determined by:

$$n = -\frac{1}{6} \left(9.0 - \frac{\sin^{1/3} \gamma}{0.14 + (b/L)} \right). \quad (28)$$

Correlation (27) fits to numerical results for $\text{Ra}^* = 10^{-2}$ to 10^5 , $0 \leq \Theta \leq 60^\circ$, $0 \leq \gamma \leq 30^\circ$, and $b/L = 0.03$ to 0.25 , with an average error about 6 %.

Second part. TURBULENT FLOW

Figure 7 shows a comparison between results obtained in this work and those reported by using the $k - \varepsilon$ turbulence model by Akbari and Borgers [24] and Chen [25], for asymmetrical heating conditions. Although the results presented show a similar trend, some differences can be observed, mainly with respect to the results presented by Chen [25], for high Ra^* . These differences may be due to the fact that Chen [25] analyzed a different configuration, including specific horizontal inlet and outlet regions. From an applied point of view, our study are focused on systems of channels with roughly Trombe wall or solar chimney geometries. In the majority of cases, the flow established in these solar passive systems becomes transitional or even fully turbulent.

Versteegh and Nieuwstadt [4] studied the flow induced by natural convection in a vertical channel with a temperature difference between isothermal walls of 39.1°C , enough to reach the turbulent regime with the geometrical and physical conditions considered. The simulations were carried out through direct numerical simulation (DNS), imposing in the inlet and outlet periodicity conditions. In this way they avoid resolving the transition from laminar

regime to turbulent regime. Aiming to validate their numeric results, the authors present experimental results of some of the analysed cases. Figure 8 shows the profiles of nondimensional velocity obtained with DNS and experimentally by Versteegh and Nieuwstadt [4], and also the profiles obtained in this work by means Fluent and Phoenics codes. It can be observed a good agreement between our results and those obtained experimentally.

Habib et al. [26] have carried out velocity measurements for natural convection flow in symmetrically and asymmetrically heated vertical channels. Results were performed using a laser Doppler anemometer. They have presented results of velocity profiles at different sections of the channel and they have compared these results with those proposed by Miyamoto et al. [10]. The Rayleigh number (defined in function of the length of the channel) was equal to 4×10^6 . Some of their results, as the results obtained in this study for the same case, are presented in Figure 9.

In view of the results obtained, the $k - \omega$ model for low-Reynolds numbers seems to simulate correctly the turbulence established by natural convection, adjusting to the available experimental results with a reasonable agreement.

In high turbulent flows induced by natural convection in channels, thermal boundary layers close to both walls are very thin and they practically do not interfere one to each other. In this way, the core region remains mainly unheated, and the heat transfer rate do not depend on inter-plate spacing. Described behavior is not reproduced for mass flow rate, probably due to the larger velocity gradients reached in turbulent boundary layers, which carry away, near enough to these shear-wall layers, an appreciable amount of fluid, arising out of the core region. This behavior reveals a relevant influence of viscosity even into regions relatively detached from walls. So, since mass flow rate have been obtained by across integration of velocity profile, aspect ratio appears as an outstanding parameter.

The following considerations about the form of correlations can be made. In literature, correlations for average Nusselt number (based on b) have been reported usually as a function of Ra^* , for laminar flow. For turbulent cases, as widely employed practice, the thermic behavior of flow has been assimilated to that corresponding to an isolated plate, i.e., assuming that influence of inter-plate spacing of the channel is negligible. Somehow, since thermal boundary layer is very thin for fully turbulent flow, best correlation of average Nusselt number (based on L) might be based on Ra_L . As aforementioned, in this work, a different behavior of turbulent velocity boundary-layer, has been observed. Thus, it can be expected the next

correlation form for the mass flow rate $\Phi \sim \mathcal{A} (\text{Ra}^*(b/L)^C)^{\mathcal{B}}$.

The results obtained for mass flow rate in vertical channels varying Ra^* from 10^4 to 10^{12} have been reported in Figure 10, for values of aspect ratio from 0.03 to 0.25. It can be observed that results obtained using both Fluent and Phoenics codes follow a same trend. The following correlation fits to numerical results obtained with Fluent:

$$\Phi = \mathcal{A} \left(\text{Ra}^*(b/L)^C \right)^{\mathcal{B}}, \quad (29)$$

with $\mathcal{A} = 0.2$, $\mathcal{B} = -0.544$ and $C = 0.54$. For $10^7 \leq \text{Ra}^* \leq 10^{12}$, average deviation between numerical results and above expression is equal to 7 %.

4.5 Influence of sloping angle

In this paragraph, influence of the sloping angle of the centerline of the channel on air mass flow rate will be described, for turbulent cases. In the results obtained through this research, it can be observed that as the sloping angle increases, the difference between the turbulence intensity generated in the lower plate with respect to that generated in the upper one, increases too. It can also be appreciated an asymmetrical field of velocity in the channel exit. Anyhow, results obtained fit an expression like (29), including $(\text{Ra}^* \cos \Theta)$ instead of Ra^* . This can be observed in Figure 11.

4.6 Influence of converging angle

Figure 12 shows results obtained for Φ as a function of Ra^* and γ . In this figure it can be appreciated a change of trend in the results of Φ for a Ra^* of the order of 10^5 , for $b/L = 0.1$ and $\Theta = 0^\circ$, agreeing with the statements by Churchill and Chu [27], which summarise the transition from laminar to turbulent regime for vertical plates in $\text{Ra}_L \approx 10^9$ (note that for $\text{Ra}^* = 10^5$ and $b/L = 0.1$, $\text{Ra}_L = \text{Ra}^* \times (b/L)^4 = 10^9$). In this way, according with above papers analysed, the roughly limit $\text{Ra}_L = 10^9$ can be accepted as good for transitional point from laminar to turbulent flow, for isolated plate and for channels with high aspect ratio, taking into account some light deviations caused by geometrical parameters (as sloping angles). The influence of the initial turbulence intensity considered will be exposed later. Results obtained fit an expression like (29), including $(\text{Ra}^* \cos \gamma)$ instead of Ra^* . This can be observed in Figure 12.

4.7 Influence of slope and converging angles. Generalized correlation

In order to obtain the influence of the sloping angle on the buoyancy-induced mass flow rate in convergent channels for turbulent regime, the cases presented have been solved for converging angles of $\gamma = 15^\circ$ and 30° , and for different sloping angles of the channel with regards to the vertical: $\Theta = 15^\circ, 30^\circ, 45^\circ$ and 60° . Once again, the factor $(\cos \Theta \cos \gamma)$ leads to obtain the overlapping of results (see Figure 13).

The results obtained for non-dimensional mass flow rate in turbulent regime induced by natural convection within of a channel with symmetrical heating, including the effects of aspect ratio, sloping and convergence angles, can be collated by the following correlation (see Figure 13):

$$\Phi = \mathcal{A} \left[\text{Ra}^* \cos \Theta \cos \gamma (b/L)^C \right]^{\mathcal{B}}, \quad (30)$$

also with $\mathcal{A} = 0.2$, $\mathcal{B} = -0.544$ and $C = 0.54$, for $10^7 \leq \text{Ra}^* \leq 10^{12}$, $0^\circ \leq \gamma \leq 30^\circ$, $0^\circ \leq \Theta \leq 60^\circ$, and for the wide range of values of b/L studied. The average error was equal to 6.4 %. Note that rearranging Equations (25) and (30) as a function of Rayleigh number based on L , leads to $\Phi \sim \text{Ra}_L^{-0.646} (b/L)^{-2.584}$, and $\Phi \sim \text{Ra}_L^{-0.544} (b/L)^{-2.470}$, for laminar boundary-layer regime, and fully-developed turbulent flow, respectively. While dependence on Rayleigh number changes significantly (19 %), the exponents obtained for b/L are similar (a discrepancy of 4.6 %), so, the influence of aspect ratio on the non-dimensional mass flow rate is mainly the same, for both boundary-layer laminar and fully turbulent regimes.

4.8 Influence of turbulence intensity

In Figure 14, numerical results have been compared with those obtained experimentally by Miyamoto et al. [10], for a channel of $L = 5$ m, $b = 95$ mm, with asymmetrical heating. One plate has been remained adiabatic, while in the other one a heat flux equal to 208 W/m^2 has been imposed. In this way, this case corresponds to $\text{Ra}_L = 5 \times 10^{14}$. For a low value of turbulence intensity, $I = 2\%$, a change of trend in results obtained for local Nusselt number Nu_x seems to indicate the transition to turbulent flow at a section next to channel outlet. Experimental results show that transition occurs at a preceding section. It is possible to fit numerical results to experimental results by means of adjusting the turbulence intensity. Indeed, best agreement with regards to experimental data reached was for $I = 2.5\%$. For higher values of I ($I = 5\%, 10\%$), the flow becomes fully turbulent, and numerical results obtained were greater

than those obtained by Miyamoto et al. [10].

For the same case, Figure 15 shows the distribution of temperature at the heated wall, at $y^+ \cong 0.3$, respectively. For $I = 2\%$, maximum value of temperature was reached for $Ra_x \cong 3.1 \times 10^{13}$; afterwards, a significant change of trend takes place, and for $Ra_x \cong 2.3 \times 10^{14}$, results merge to those obtained for $I = 0.05$ and $I = 0.1$, i.e., for fully turbulent flow. For $I = 2.5\%$, critical points take place at preceding sections ($Ra_x \cong 9.5 \times 10^{12} - 7.1 \times 10^{13}$), and for $I = 5\%$, the flow was fully turbulent, as pointed above. For high values of I (5%, 10%), the lower values reached for temperature at along the wall, for a same value of heat flux imposed, lead to obtain greater average Nusselt numbers.

Fedorov and Viskanta [9] showed the strong influence exerted by the turbulence intensity in the local heat transfer at the inlet of the channel. They presented distributions of the local Nusselt number along the wall of an isothermal channel with symmetrical heating, for $Gr_b = 2 \times 10^5, 4 \times 10^5, 6 \times 10^5$ and 10^6 , and $I = 0, 10$ and 30% . Their results shown that for $Gr_b = 4 \times 10^5$ and $I = 0$, the flow evolved from laminar to turbulent at $x/L = 0.84$. As the Grashof number was increased further, the transitional point moved closer to the inlet; for $Gr_b = 10^6$, the transition was takes place at $x/L = 0.64$. An increase in the intensity of turbulence at the inlet of channel yielded an advance in transition. At the moment, results obtained in present work have reproduced the same behavior. However, since above cases of Fedorov and Viskanta [9] have been simulated in this work, some difference can be appreciated (see Figure 16). In fact, laminar flow remains for $Gr_b = 2, 4$ and 6×10^5 , transition occurs for $Gr_b = 10^6$, and higher values of I yield a strong turbulent flow for the same value of $Gr_b = 10^6$. For $I = 30\%$, average Nusselt number was a 31% higher than corresponding value to $I = 0$, for $Gr_b = 10^6$.

In this way, an important aspect on design considerations is to fixe the suitable turbulent excitation so as to obtain transition to turbulence; however, a meaningful physical flow must be maintained. In thermal passive systems, no external mechanical devices are employed. Indeed, a low value of initial turbulence at inlet must be considered, since it is not expected additional turbulence generating.

In order to study the influence of I in a more systematic way, results for average Nusselt number based on L , Nu_L , have been obtained in a vertical channel ($\gamma = \Theta = 0^\circ$), for turbulence intensity $I = 0.02, 0.05, 0.1$ and 0.2 , a range of Rayleigh number $10^6 \leq Ra_L \leq 10^{16}$, a fixed value of aspect ratio equal to 0.2 , and isothermal symmetric heating. The results show (see Figure

17) that the bigger the turbulence intensity in the entrance, the bigger the flow mixing in the inlet zone and the local transition between laminar regime and turbulent regime is less brusque. In this way, as expected, turbulence transition may occur for low local Grashof (or Rayleigh) number, if a great turbulence excitation is imposed at inlet. These differences lead to a maximum deviation for the average Nusselt number close to 18% between one case with $I = 2\%$ and other with $I = 20\%$, for the Rayleigh numbers considered in a transitional range ($Ra_L = 10^9$). These differences are really significant in a given range of the Rayleigh number ($Ra_L = 5 \times 10^7 - 5 \times 10^{10}$) within the set of the laminar-turbulent transition. These effects were much more important on the induced mass flow rate through the channel (Figure 18). It can be explained by the different influence of turbulence effects over shear and thermal boundary layers, respectively. For Ra_L in the transitional zone, although flow pattern and velocity boundary layer shown a similar aspect close to the wall for different values of initial turbulence intensity I , the fluid was compelled to move in the core region in a more significant way for higher values of I (see Figure 19). This fact leads to obtain a drastic increase in the mass flow rate. In this way, these important differences produce also to a change in the evolution of non-dimensional mass flow rate Φ as a function of Ra_L for $Ra_L > 10^9$, and, for high enough values of Ra_L , the trend becomes to be identical that those corresponding to strong turbulence flow. For example, for $Ra_L = 10^9$, deviations with regards to $I = 2\%$ case were equal to 65%, 110% and 150%, for $I = 5\%$, $I = 10\%$, and $I = 20\%$, respectively. While, for $Ra_L = 10^{10}$, deviations were equal to 29%, 40% and 47%, respectively. The differences are lower for fully turbulent flow, as expected. For $Ra_L \geq 10^{13}$, deviations reached almost negligible, and results obtained have not been shown in Figures 17 and 18.

Finally, change of trend between asymptotic laminar and fully turbulent behaviors, which clearly can be observed in Figure 17 for average Nusselt number, do not appears in Figure 18 for the non-dimensional mass flow rate Φ .

5 Concluding remarks

Buoyancy-driven flows in channels for whole range of Rayleigh numbers, and for different converging and centerline sloping angles, have been analyzed. Most of cases were solved for isothermal symmetric heating conditions. The low-Reynolds $k - \omega$ turbulence model has been validated through experimental and numerical results proposed by Versteegh and

Nieuwstadt [4], Miyamoto et al. [2], and Habib et al. [26]. It has been obtained the non-dimensional mass flow rate for modified Rayleigh numbers $10^{-2} \leq Ra^* \leq 10^{12}$, aspect ratios $0.03 \leq b/L \leq 0.25$, converging angles $0^\circ \leq \gamma \leq 30^\circ$, sloping angles $0^\circ \leq \Theta \leq 60^\circ$, and initial turbulence intensities $0 \leq I \leq 30\%$, although most of results was obtained for $I = 2\%$.

The following concluding remarks can be made:

1. The numerical results for turbulent flow have been linked with the laminar ones obtained in a previous research, Kaiser et al. [17].
2. For turbulent flow, the results obtained showed that aspect ratio b/L influences on non-dimensional mass flow rate Φ in a significant way.
3. For sloping and convergent channels, the results for the non-dimensional mass flow rate Φ can be fitted to those obtained for vertical channels by modification of Rayleigh number through the geometric factor ($\cos \Theta \cos \gamma$).
4. A generalized correlation for Φ has been reported, valid for the wide range of modified Rayleigh number outlined, involving laminar and turbulent regimes, for a low value of initial turbulence intensity ($I = 2\%$ for the turbulent cases), aspect ratios $0.03 \leq b/L \leq 0.25$, and $0 \leq \gamma \leq 30^\circ$, $0 \leq \Theta \leq 60^\circ$.
5. Finally, effects of turbulence intensity at inlet of the channel, were much more important on non-dimensional mass flow rate than on average Nusselt number, in the transitional range. High values of initial turbulence intensity yielded an advance on the transitional Rayleigh number, while low values of I produced a significant deviation from asymptotic behavior corresponding to strong turbulent flow.

6 Acknowledgement

This research has been supported by the 'Dirección General de Investigación' of 'Ministerio de Educación y Ciencia' of Spanish Government, through DPI 2003-02719 Project.

References

- [1] J. R. Lloyd, E. M. Sparrow, On the instability of natural convection flow on inclined plates, *J. Fluid Mech.* 42 (1970) 465–470.
- [2] M. Miyamoto, Y. Katoh, J. Kurima, Turbulent free convection heat transfer from vertical parallel plates in air (heat transfer characteristics), *NACSIS Electronic Library Service* 1 (1983) 1–7.
- [3] X. Yuan, A. Moser, P. Suter, Wall functions for numerical simulation of turbulent natural convection along vertical plates, *Int. J. Heat Mass Transfer* 36 (1993) 4477–4485.
- [4] T. A. Versteegh, F. T. Nieuwstadt, A direct numerical simulation of natural convection between two infinite vertical differentially heated walls scaling laws and wall functions, *Int. J. Heat Mass Transfer* 42 (1999) 3673–3693.
- [5] R. A. W. M. Henkes, C. J. Hoogendorn, Comparison exercise for computations of turbulent natural convection in enclosures, *Numerical Heat Transfer* 28 (1995) 59–78.
- [6] S. Peng, L. Davison, Computation of turbulent buoyant flows in enclosures with low-reynolds number $k - \omega$ models, *Int. J. Heat Fluid Flow* 20 (1999) 172–184.
- [7] W. Xu, Q. Chen, F. T. M. Nieuwstadt, A new turbulence model for near wall natural convection, *Int. J. Heat Mass Transfer* 41 (1998) 3161–3176.
- [8] S. A. M. Said, M. A. Habib, H. M. Badr, S. Anwar, Turbulent natural convection between inclined isothermal plates, *Computers and Fluids* 34 (2005) 1025–1039.
- [9] A. G. Fedorov, R. Viskanta, Turbulent natural convection heat transfer in an asymmetrically heated, vertical parallel-plate channel, *Int. J. Heat Mass Transfer* 40 (1997) 3849–3860.
- [10] M. Miyamoto, Y. Katoh, J. Kurima, H. Suki, Turbulent free convection heat transfer from vertical parallel plates, in *Heat Transfer*, Eds. C.L. Tien, V.P. Carey and J.K. Ferrel, Hemisphere, Washington D.C. 4 (1986) 1593–1598.
- [11] A. Hajji, W. M. Worek, Analysis of combined fully developed natural convection heat and mass transfer between two inclined parallel plates, *Int. J. Heat Mass Transfer* 31 (1988) 1933–1940.

- [12] K. T. Lee, Natural convection in vertical parallel plates with an unheated entry or an unheated exit, *Numerical Heat Transfer* 25 (1994) 477–493.
- [13] W. Aung, Fully developed laminar free convection between vertical plates heated asymmetrically, *Int. J. Heat Mass Transfer* 15 (1972) 1577–1580.
- [14] D. J. Nelson, B. D. Wood, Fully developed combined heat and mass transfer natural convection between parallel vertical plates with asymmetric boundary conditions, *Int. J. Heat Mass Transfer* 32 (1989) 1789–1792.
- [15] Z. Y. Guo, X. B. Wu, Thermal drag and critical heat flux for natural convection of air in vertical parallel plates, *ASME J. Heat Transfer* 115 (1993) 124–129.
- [16] J. Hernández, B. Zamora, Effects of variable properties and non-uniform heating on natural convection flows in vertical channels, *Int. J. Heat Mass Transfer* 48 (2005) 793–807.
- [17] A. S. Kaiser, B. Zamora, A. Viedma, Correlation for nusselt number in natural convection in vertical convergent channels at uniform wall temperature by a numerical investigation, *Int. J. Heat Fluid Flow* 25 (2004) 671–682.
- [18] D. C. Wilcox, *Turbulence Modeling for CFD*, 2nd ed., DCW Industries, USA, 2003.
- [19] A. N. Kolmogorov, Equations of turbulent motion of an incompressible fluid, *Izvestia Academy of Sciences, USSR, Physics* 6 (1942) 56–58.
- [20] J. Hernández, B. Zamora, A. Campo, On the effect of Prandtl number and aspect ratio upon laminar natural-convection flows in vertical channels, *Proc. Tenth International Heat Transfer Conference* 5 (1994) 483–488.
- [21] S. V. Patankar, D. B. Spalding, A calculation procedure for heat, mass and momentum transfer in three-dimensional parabolic flows, *Int. J. Heat Mass Transfer* 15 (1972) 1787–1806.
- [22] B. Van Leer, Towards the ultimate conservative difference scheme V. A second order sequel to Godunov's method, *J. Comput. Phys.* 32 (1979) 101–136.
- [23] S. W. Churchill, J. F. Usagi, A general expression for the correlation of rates of transfer and other phenomena, *AIChE Y.* 18 (1972) 1121–1128.

- [24] H. Akbari, T. R. Borgers, Free convective turbulent flows within the trombe wall channel, *Solar Energy* 33 (1984) 253–264.
- [25] T. Chen, Laminar and Turbulent Natural Convection Heat Transfer in Trombe Wall Channels, PhD thesis, University of Old Dominion, 1992.
- [26] M. A. Habib, S. A. M. Said, S. A. Ahmed, A. Asghar, Velocity characteristics of turbulent natural convection in symmetrically and asymmetrically heated vertical channels, *Experimental Thermal of Fluid Science* 26 (2002) 77–87.
- [27] S. W. Churchill, H. H. S. Chu, Correlating equations for laminar and turbulent free convection from a vertical plate, *Int. J. Heat Mass Transfer* 18 (1975) 1323.

Captions for figures

Figure 1: Scheme of a converging sloped channel formed by isothermal AC and BD walls.

Figure 2: Influence of number of cells and y^+ values on numerical results. $Ra^* = 10^9$, $b/L = 0.1$, $\gamma = 12^\circ$, $\Theta = 0^\circ$.

Figure 3: Non-dimensional mass flow rate Φ as a function of modified Rayleigh number Ra^* and sloping angle Θ , for a channel with isothermal heating, converging angle $\gamma = 0^\circ$, and aspect ratios $b/L = 0.03$ and 0.1 . Hajji and Worek [11] asymptote for vertical channel and fully developed flow.

Figure 4: Non-dimensional mass flow rate Φ as a function of modified Rayleigh number Ra^* and converging angle γ , for a channel with isothermal heating, sloping angle $\Theta = 0^\circ$, and aspect ratio $b/L = 0.1$. Hajji and Worek [11] asymptote for vertical channel and fully developed flow.

Figure 5: Non-dimensional mass flow rate Φ as a function of $Ra^*(\cos \Theta)(\cos \gamma)$, for a channel with isothermal heating, $\gamma = 30^\circ$, $\Theta = 15^\circ, 30^\circ, 45^\circ, 60^\circ$, and aspect ratio $b/L = 0.1$. Hajji and Worek [11] asymptote for vertical channel and fully developed flow.

Figure 6: Global correlation for non-dimensional mass flow rate as a function of $Ra^*(\cos \Theta)(\cos \gamma)$ and converging angle γ , for a channel with isothermal heating, $\Theta = 0^\circ$ and $b/L = 0.1$.

Figure 7: Comparison of non-dimensional mass flow rate obtained by Akbari and Borgers [24], and Chen [25], and those obtained in this work, for a channel with asymmetric heating conditions and turbulent flow. $\gamma = \Theta = 0^\circ$.

Figure 8: Comparison between velocity profiles obtained in this work (using Fluent and Phoenics codes) with those obtained by Versteegh and Niewstadt [4], for a vertical channel with isothermal heating. $\gamma = \Theta = 0^\circ$. $b/L = 1/28.6$ and $b = 0.076$ mm.

Figure 9: Comparison of velocity profiles obtained in this research (using Fluent and Phoenics codes) with those proposed by Miyamoto et al. [10] and those reached by Habib et al. [26] for a vertical channel with $Ra_L = 4 \times 10^6$, being \bar{U} the average velocity in the channel. $\gamma = \Theta = 0^\circ$. $L = 0.125$ m and $b = 0.04$ m.

Figure 10: Non-dimensional mass flow rate as a function of Ra^* for different values of b/L . Isothermal channel with symmetrical heating. $\gamma = \Theta = 0^\circ$.

Figure 11: Influence of sloping angle over non-dimensional mass flow rate in an inclined channel. Symmetrical heating conditions. Numerical correlation proposed. $\gamma = 0^\circ$, $b/L = 0.1$.

Figure 12: Influence of converging angle over non-dimensional mass flow rate, as a function of Ra^* . Symmetrical heating conditions. $\Theta = 0^\circ$, $b/L = 0.1$. Hajji and Worek [11] asymptote for vertical channel and fully developed flow.

Figure 13: Overlapping of results obtained for non-dimensional mass flow rate, for turbulent flow. Channel with isothermal symmetric heating conditions.

Figure 14: Comparison with experimental results reported by Miyamoto et al. [2], for an isothermal asymmetrically-heated channel, imposing a heat flux at one of walls equal to 208 W/m^2 , and $b = 95 \text{ mm}$, $L = 5 \text{ m}$, $Ra_L = 5 \times 10^{14}$. $\gamma = \Theta = 0^\circ$.

Figure 15: Evolution of temperature along heated wall for an isothermal asymmetrically-heated channel, imposing a heat flux at one of walls equal to 208 W/m^2 , and $b = 95 \text{ mm}$, $L = 5 \text{ m}$, $Ra_L = 5 \times 10^{14}$, for different values of turbulence intensity I . $\gamma = \Theta = 0^\circ$.

Figure 16: Distribution of local Nusselt Number along heated wall for an isothermal channel with symmetrical heating, for different values of Gr_b and turbulence intensity I . Average Nusselt number obtained for each case has been also indicated. $\gamma = \Theta = 0^\circ$, $b/L = 0.0125$.

Figure 17: Average Nusselt number Nu_L as a function of Ra_L . Influence of turbulence intensity I on the transitional range of Ra_L . Channel with isothermal heating conditions. $\gamma = \Theta = 0^\circ$. $b/L = 0.2$.

Figure 18: Non-dimensional mass flow rate Φ as a function of Ra_L . Influence of turbulence intensity I on the transitional range of Ra_L . Channel with isothermal heating conditions. $\gamma = \Theta = 0^\circ$. $b/L = 0.2$.

Figure 19: Profils of mean velocity at outlet of a channel with isothermal heating conditions, for two values of Ra_L , 10^6 and 10^{10} , showing the influence of turbulence intensity I . $\gamma = \Theta = 0^\circ$. $b/L = 0.2$.

Figures

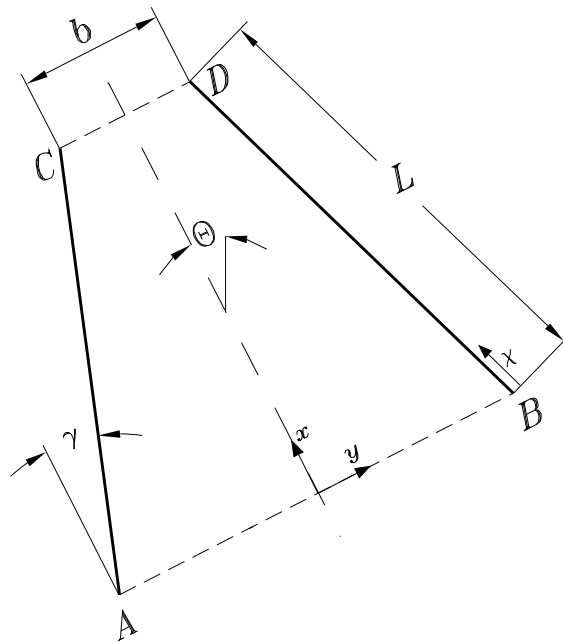


Figure 1: Scheme of a converging sloped channel formed by isothermal AC and BD walls.

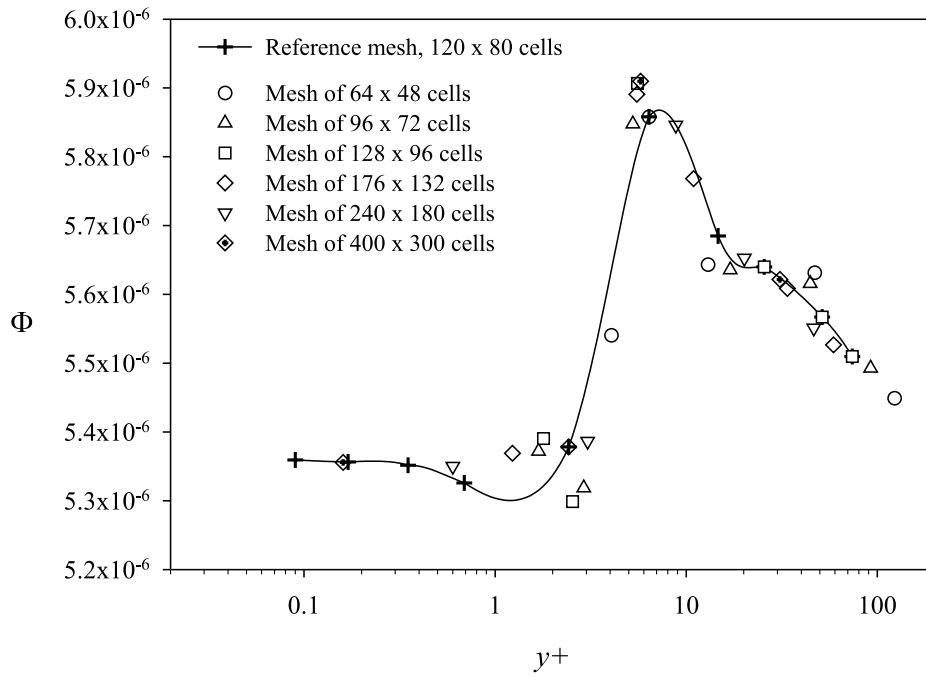


Figure 2: Influence of number of cells and y^+ values on numerical results. $Ra^* = 10^9$, $b/L = 0.1$, $\gamma = 12^\circ$, $\Theta = 0^\circ$.

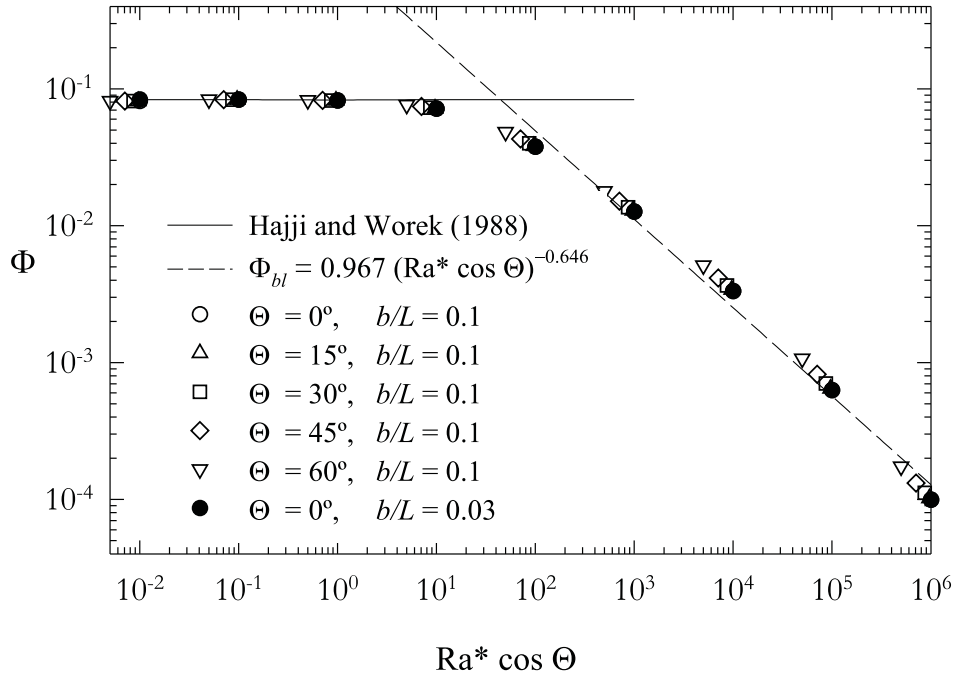


Figure 3: Non-dimensional mass flow rate Φ as a function of modified Rayleigh number Ra^* and sloping angle Θ , for a channel with isothermal heating, converging angle $\gamma = 0^\circ$, and aspect ratios $b/L = 0.03$ and 0.1 . Hajji and Worek [11] asymptote for vertical channel and fully developed flow.

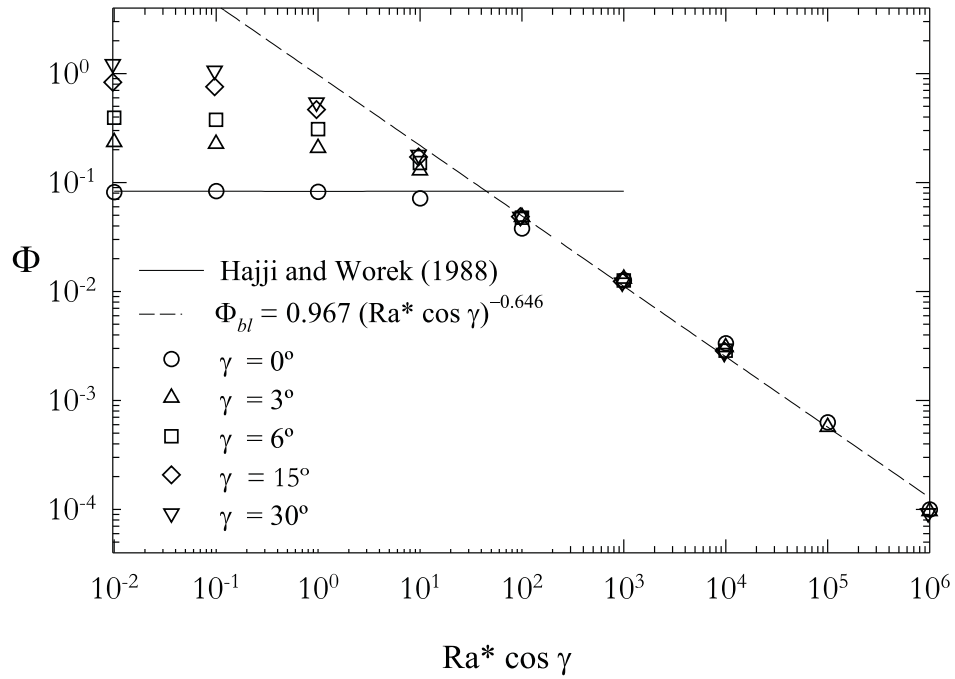


Figure 4: Non-dimensional mass flow rate Φ as a function of modified Rayleigh number Ra^* and converging angle γ , for a channel with isothermal heating, sloping angle $\Theta = 0^\circ$, and aspect ratio $b/L = 0.1$. Hajji and Worek [11] asymptote for vertical channel and fully developed flow.

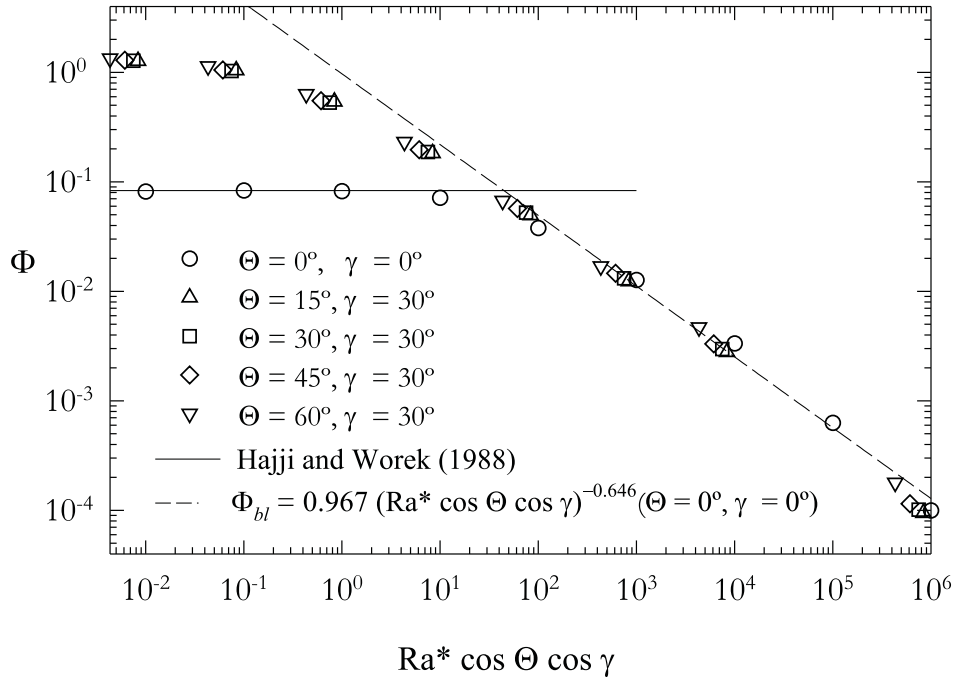


Figure 5: Non-dimensional mass flow rate Φ as a function of $Ra^*(\cos \Theta)(\cos \gamma)$, for a channel with isothermal heating, $\gamma = 30^\circ$, $\Theta = 15^\circ, 30^\circ, 45^\circ, 60^\circ$, and aspect ratio $b/L = 0.1$. Hajji and Worek [11] asymptote for vertical channel and fully developed flow.

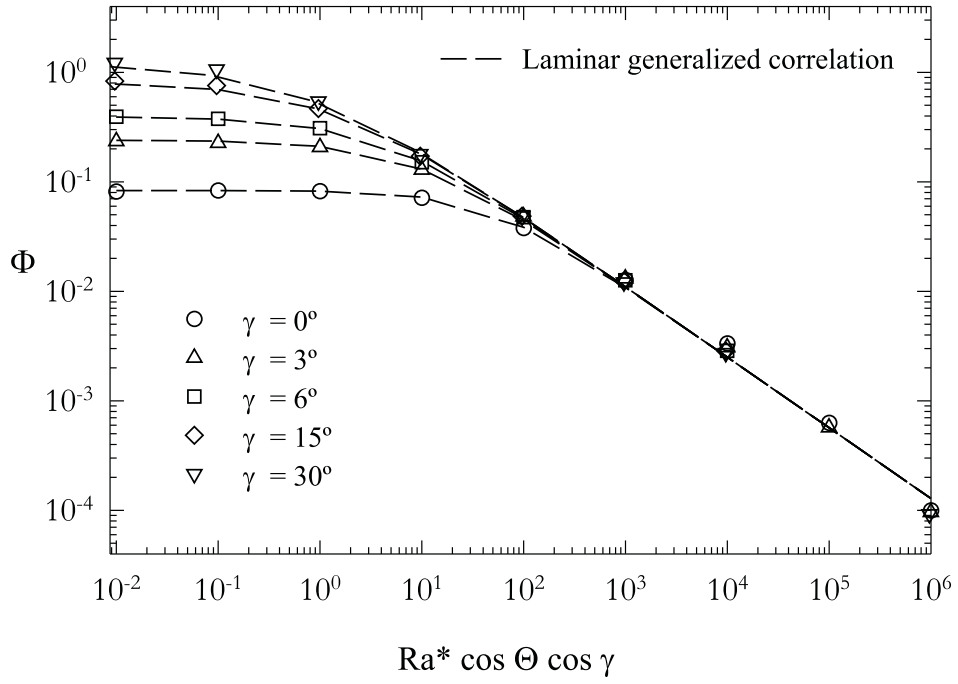


Figure 6: Global correlation for non-dimensional mass flow rate as a function of $Ra^*(\cos\Theta)(\cos\gamma)$ and converging angle γ , for a channel with isothermal heating, $\Theta = 0^\circ$ and $b/L = 0.1$.

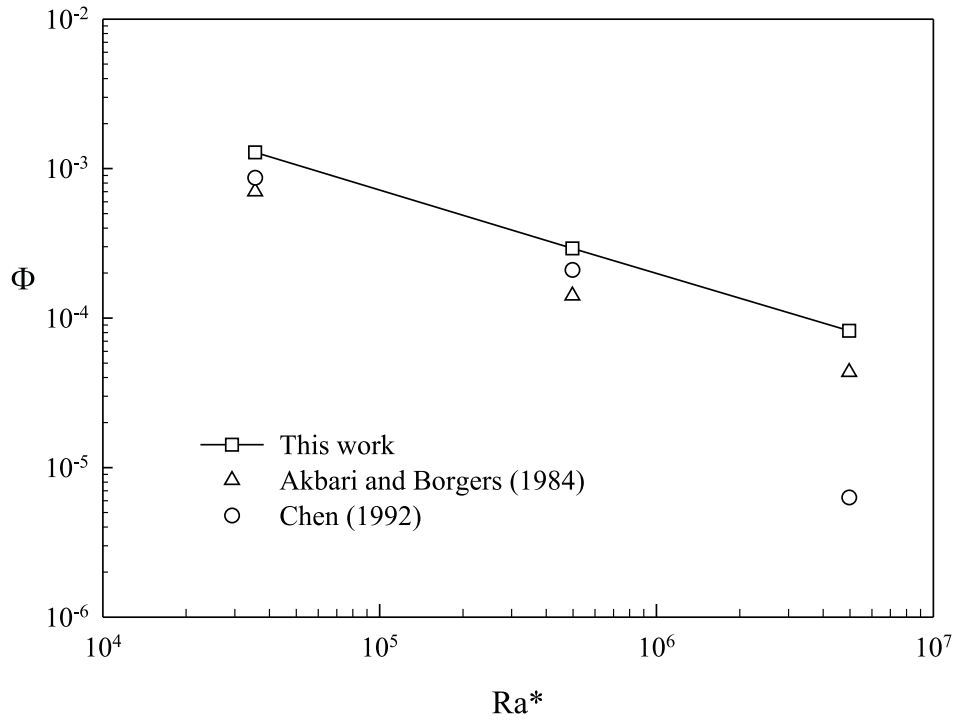


Figure 7: Comparison of non-dimensional mass flow rate obtained by Akbari and Borgers [24], and Chen [25], and those obtained in this work, for a channel with asymmetric heating conditions and turbulent flow. $\gamma = \Theta = 0^\circ$.

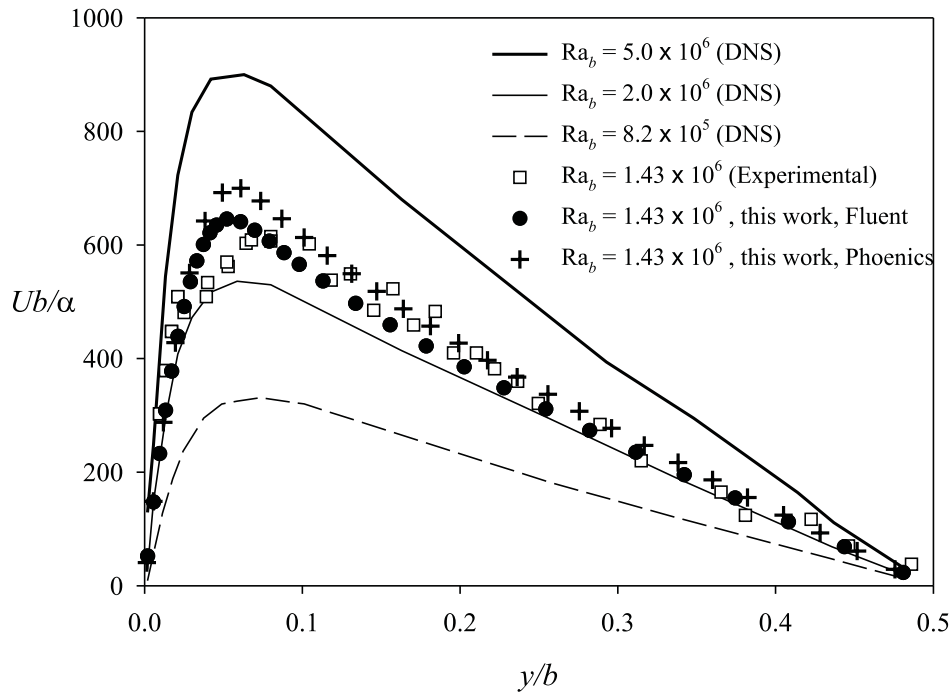


Figure 8: Comparison between velocity profiles obtained in this work (using Fluent and Phoenics codes) with those obtained by Versteegh and Niewstadt [4], for a vertical channel with isothermal heating. $\gamma = \Theta = 0^\circ$. $b/L = 1/28.6$ and $b = 0.076$ mm.

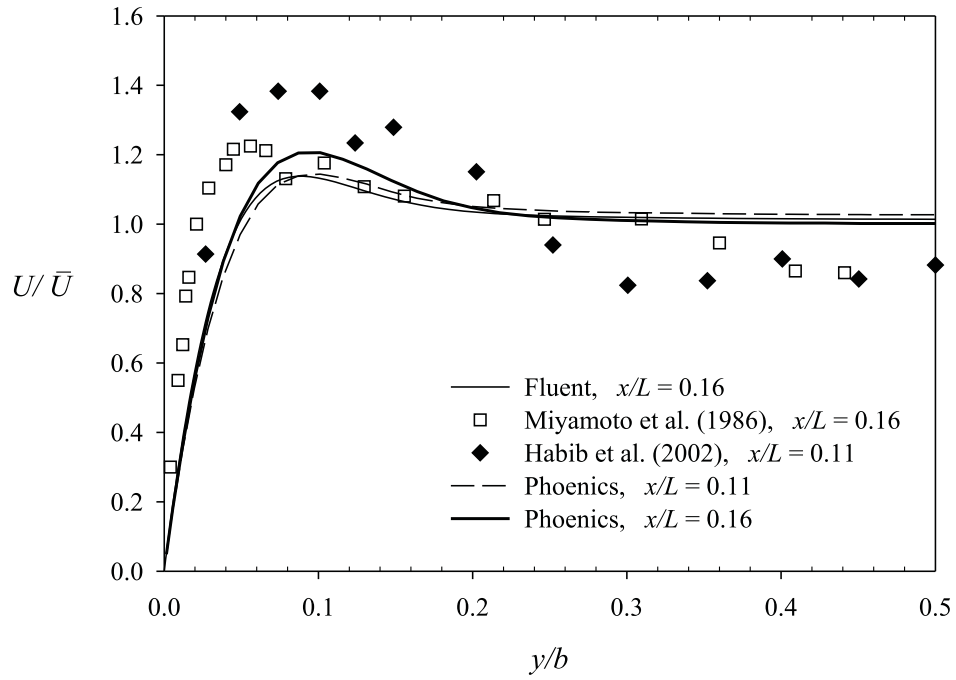


Figure 9: Comparison of velocity profiles obtained in this research (using Fluent and Phoenics codes) with those proposed by Miyamoto et al. [10] and those reached by Habib et al. [26] for a vertical channel with $Ra_L = 4 \times 10^6$, being \bar{U} the average velocity in the channel. $\gamma = \Theta = 0^\circ$. $L = 0.125$ m and $b = 0.04$ m.

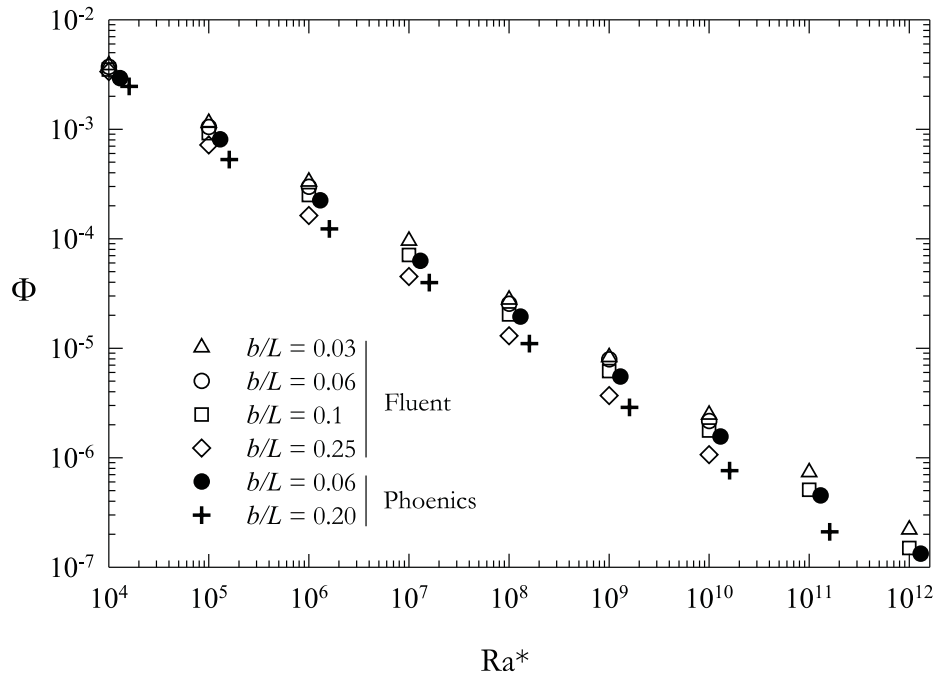


Figure 10: Non-dimensional mass flow rate as a function of Ra^* for different values of b/L . Isothermal channel with symmetrical heating. $\gamma = \Theta = 0^\circ$.

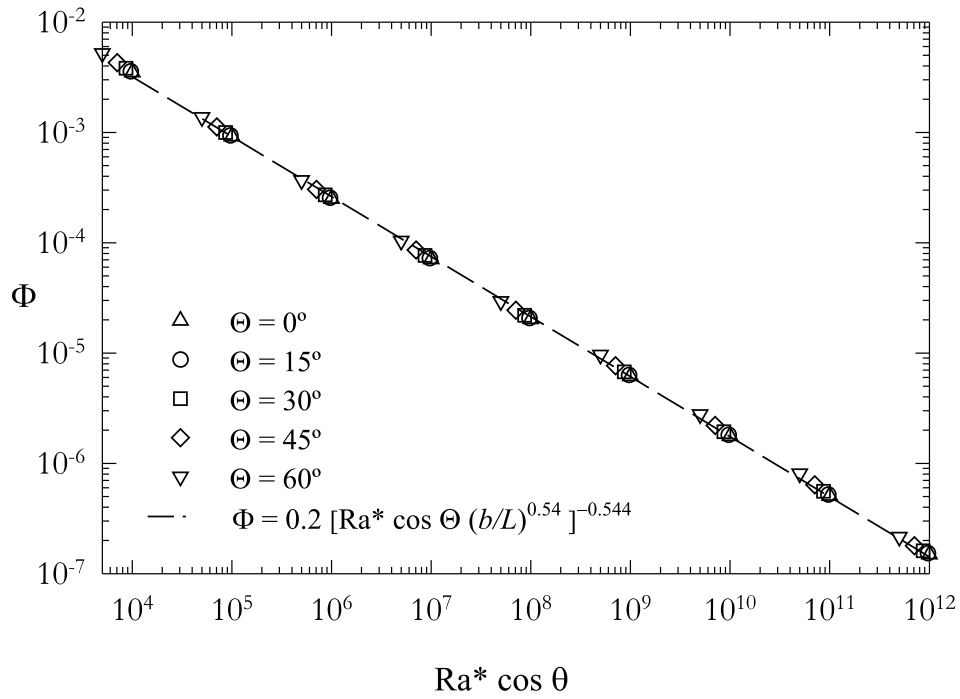


Figure 11: Influence of sloping angle over non-dimensional mass flow rate in an inclined channel. Symmetrical heating conditions. Numerical correlation proposed. $\gamma = 0^\circ$, $b/L = 0.1$.

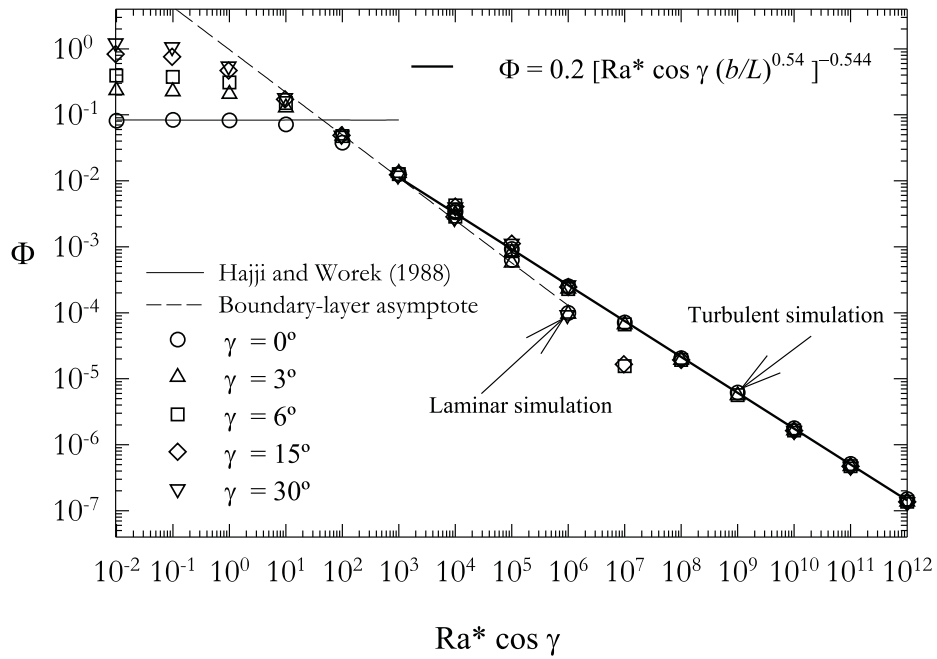


Figure 12: Influence of converging angle over non-dimensional mass flow rate, as a function of Ra^* . Symmetrical heating conditions. $\Theta = 0^\circ$, $b/L = 0.1$. Hajji and Worek [11] asymptote for vertical channel and fully developed flow.

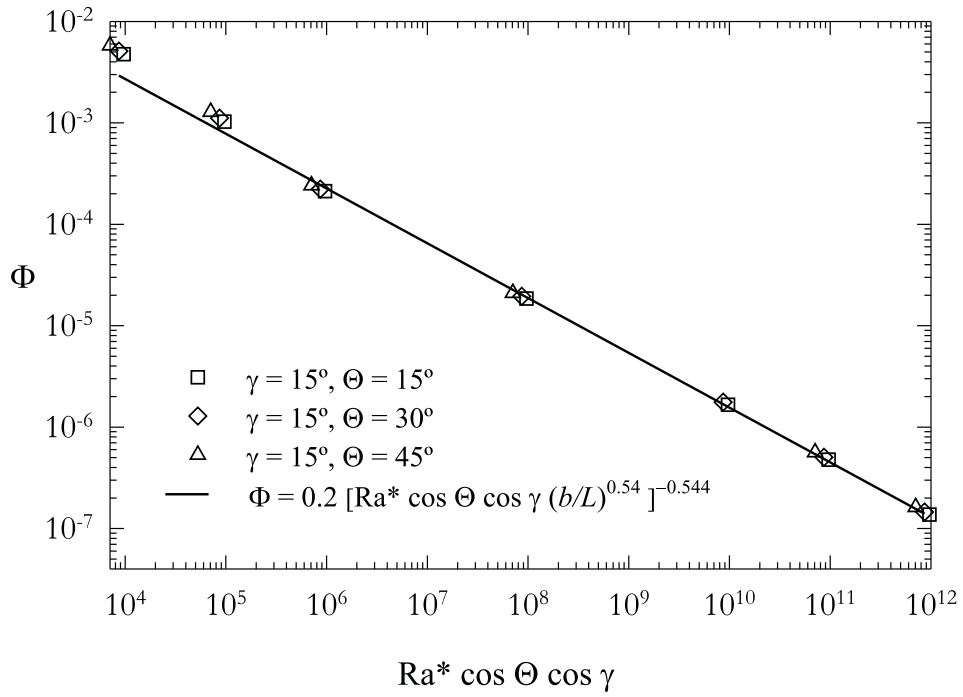


Figure 13: Overlapping of results obtained for non-dimensional mass flow rate, for turbulent flow. Channel with isothermal symmetric heating conditions.

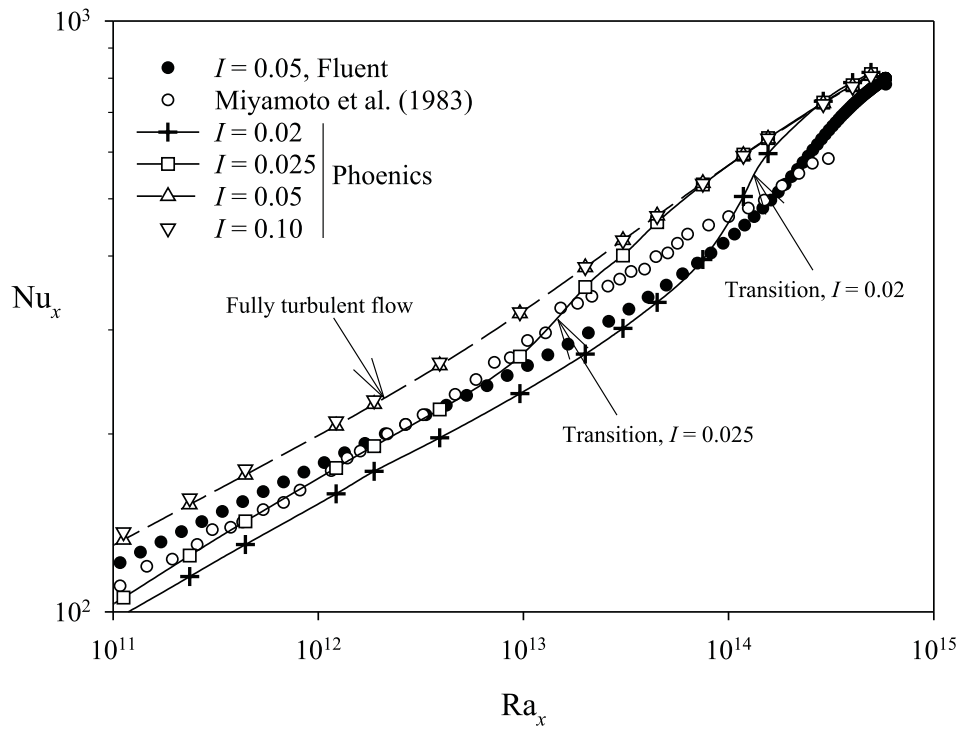


Figure 14: Comparison with experimental results reported by Miyamoto et al. [2], for an isothermal asymmetrically-heated channel, imposing a heat flux at one of walls equal to 208 W/m^2 , and $b = 95 \text{ mm}$, $L = 5 \text{ m}$, $Ra_L = 5 \times 10^{14}$. $\gamma = \Theta = 0^\circ$.

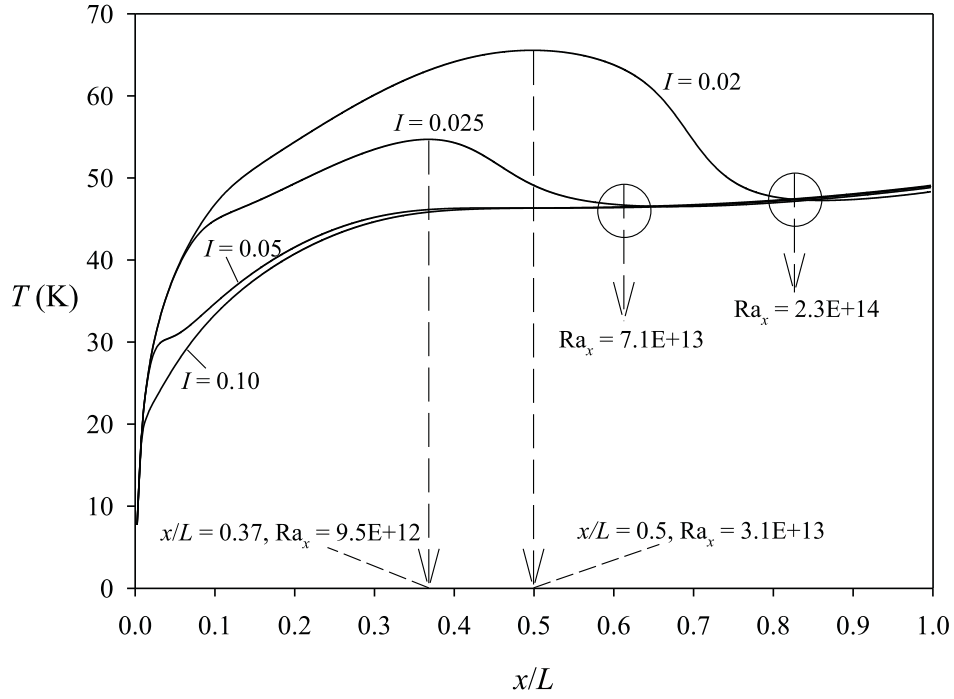


Figure 15: Evolution of temperature along heated wall for an isothermal asymmetrically-heated channel, imposing a heat flux at one of walls equal to 208 W/m^2 , and $b = 95 \text{ mm}$, $L = 5 \text{ m}$, $Ra_L = 5 \times 10^{14}$, for different values of turbulence intensity I . $\gamma = \Theta = 0^\circ$.

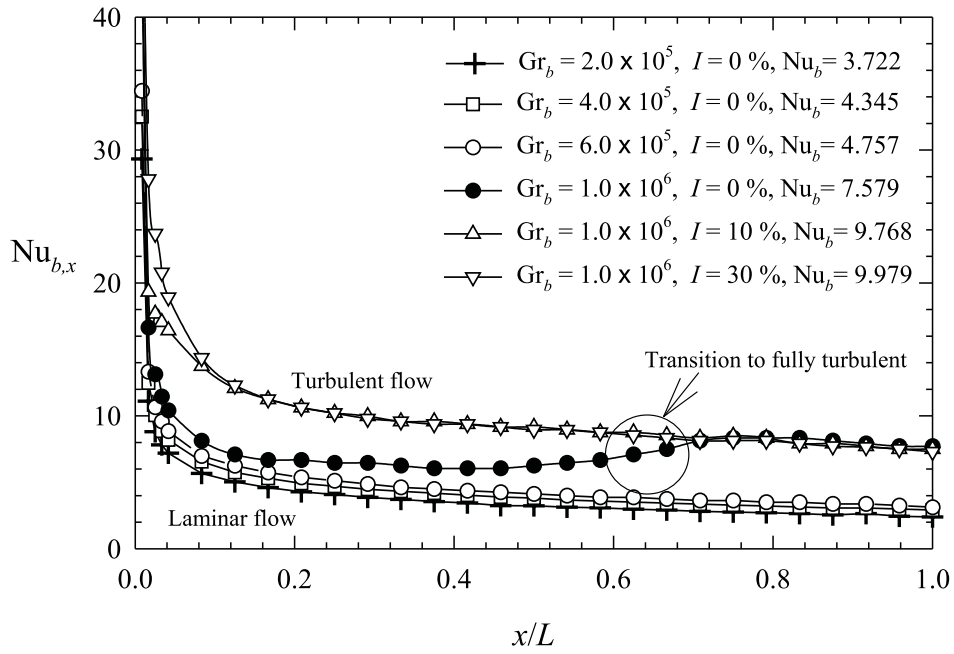


Figure 16: Distribution of local Nusselt Number along heated wall for an isothermal channel with symmetrical heating, for different values of Gr_b and turbulence intensity I . Average Nusselt number obtained for each case has been also indicated. $\gamma = \Theta = 0^\circ$, $b/L = 0.0125$.

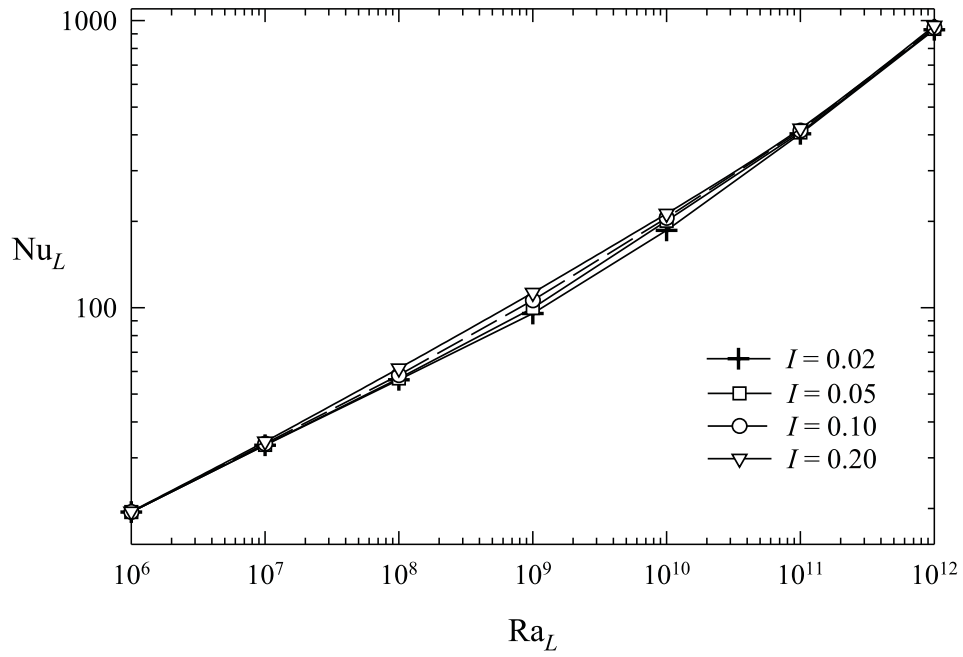


Figure 17: Average Nusselt number Nu_L as a function of Ra_L . Influence of turbulence intensity I on the transitional range of Ra_L . Channel with isothermal heating conditions. $\gamma = \Theta = 0^\circ$. $b/L = 0.2$.

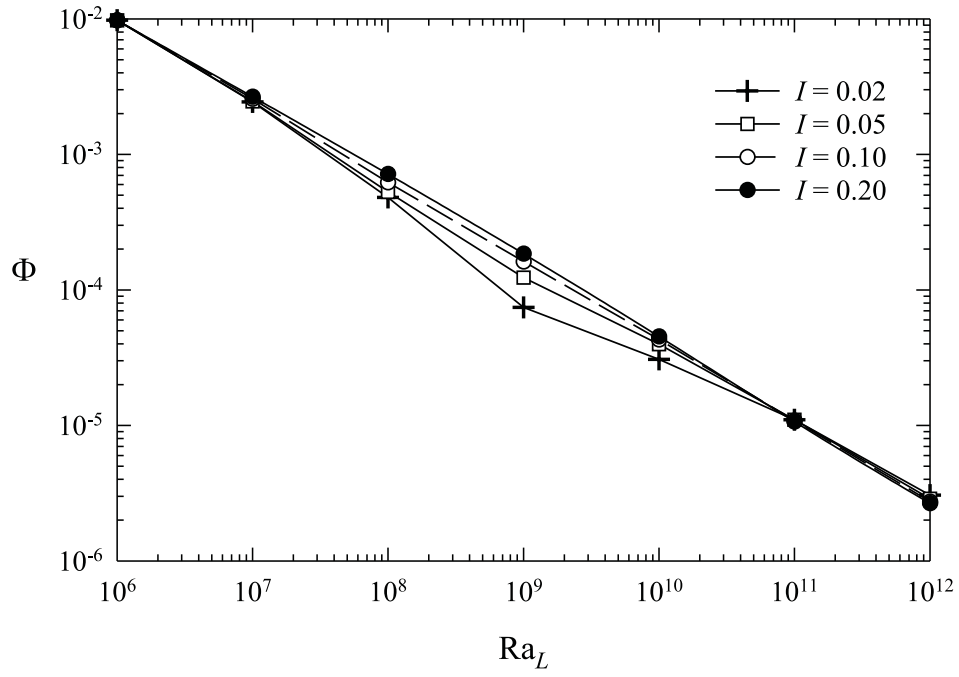


Figure 18: Non-dimensional mass flow rate Φ as a function of Ra_L . Influence of turbulence intensity I on the transitional range of Ra_L . Channel with isothermal heating conditions. $\gamma = \Theta = 0^\circ$. $b/L = 0.2$.

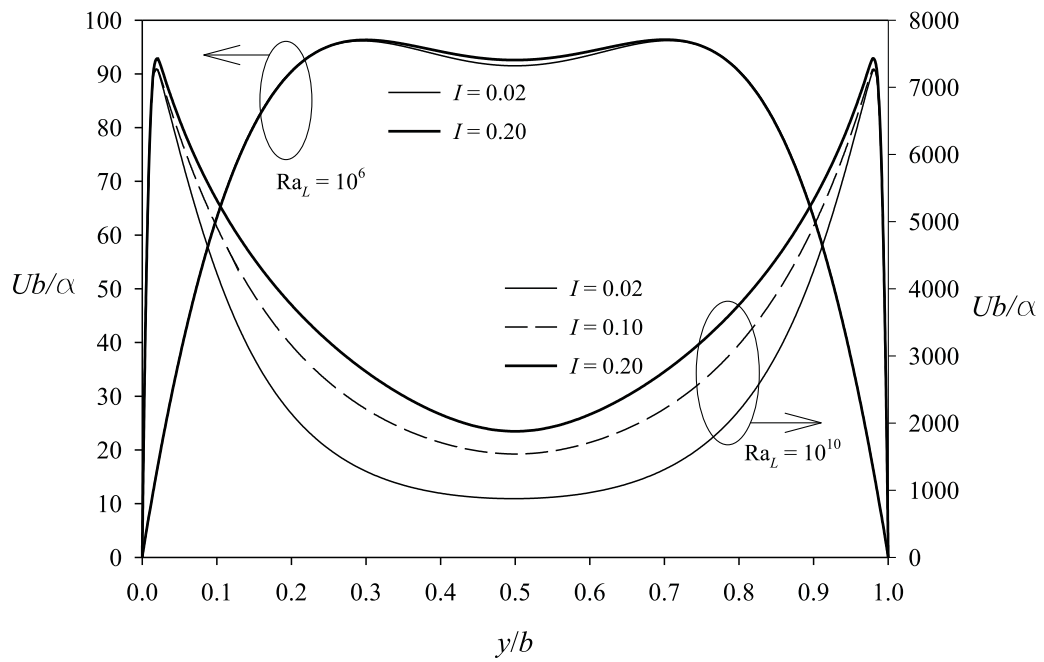


Figure 19: Profiles of mean velocity at outlet of a channel with isothermal heating conditions, for two values of Ra_L , 10^6 and 10^{10} , showing the influence of turbulence intensity I . $\gamma = \Theta = 0^\circ$. $b/L = 0.2$.